Dalton Transactions

ROYAL SOCIETY OF CHEMISTRY

PAPER

View Article Online
View Journal | View Issue

Cite this: *Dalton Trans.*, 2024, **53**, 15471

$Sr_4Al_{14}O_{25}:Li^+,Mn^{4+}$ phosphor-in-glass film: erosion behavior and luminescence property

Yunzheng Liu,[a,c] Haoyu Yang,[b] Haohui Jiang,[b] Daoyuan Ma,[a] Wenfa Fang[a] and Libin Xia*[a,b,c]

At present, phosphor-in-glass is regarded as a superior encapsulation material substituting for organic materials to resolve the poor thermal stability of WLEDs. However, the serious erosion reaction between commercial red phosphor and the glass matrix restricts the development and application of red phosphor-in-glass. In this work, a novel $Sr_4Al_{14}O_{25}:Li^+,Mn^{4+}$ (SAO) red phosphor-in-glass film (PiGF) with precursor glass xB_2O_3–$(85 - x)Bi_2O_3$–$5Al_2O_3$–10CaO was prepared using a low-temperature sintering technique. Crystallization was observed in the precursor glass with 40% and 45% B_2O_3 content at 570 °C for 30 min, with the crystalline phase mainly being $Bi_4B_2O_9$. The glass transition temperature gradually increases from 420 to 496 °C with an increase in B_2O_3 content from 40 to 60%. The DSC simulation and experimental results show that the degree of erosion of SAO phosphors decreases with an increase in B_2O_3 content from 50 to 60% and with an increase in the co-sintering temperature from 570 to 590 °C, while the glass surface smoothness of the PiGFs decreases with increasing B_2O_3 content. 55% B_2O_3 and 570 °C are the optimal parameters. The PL and PLE of the PiGFs show that the luminous intensity increases and then decreases with increasing B_2O_3 content, with 55% B_2O_3 also being the optimal value. The PiGF shows a quantum efficiency of 46.62%, and the luminous intensity maintains 85.1% of its initial intensity at 348 K.

Received 5th July 2024,
Accepted 23rd August 2024

DOI: 10.1039/d4dt01941e

rsc.li/dalton

1. Introduction

The application of commercial phosphor-conversion WLEDs (pc-LEDs) in the field of medium and high power is restricted due to their poor thermal stability ascribed to organic encapsulation.[1–3] Recently, a new material of phosphor-in-glass (PiG) with high thermal stability has been widely studied, which is regarded as an effective solution for the disadvantages of pc-LEDs.[4–6] Among these, yellow-green PiGs, prepared with $Y_3Al_5O_{12}:Ce^{3+}$ or $Lu_3Al_5O_{12}:Ce^{3+}$ phosphors and a glass matrix, have been successfully prepared and showed a superior luminous property due to the rigid garnet structure of the phosphors.[7–10] However, improving the luminescence of red PiGs is challenging due to the interactive reactions between commercial red phosphors and the glass matrix. This result originates from the structural rigidity of commercial red phosphors ($CaAlSiN_3:Eu^{2+}$, $K_2SiF_6:Mn^{4+}$ and so on) being weaker than that of a garnet structure.[11–13] Therefore, the erosion reactions between red phosphors and the glass matrix to improve the luminous property deserve to be studied in depth.

Generally, the process conditions, including glass composition, co-sintering temperature and co-sintering time, are key factors affecting the erosion reactions and luminous property of red PiGs.[14] $CaAlSiN_3:Eu^{2+}$ PiGs were prepared with glass matrices of SiO_2–Al_2O_3–Pb_2O_3, B_2O_3–Na_2O–Al_2O_3, and B_2O_3–Na_2O–SiO_2–CaO, and different temperatures have been studied to survey the vibrational luminescence properties. The results demonstrate that the luminous intensity of the $CaAlSiN_3:Eu^{2+}$ PiGs decreases gradually with increasing co-sintering temperature, which indicates that the degree of the erosion reaction increases with increasing temperature.[9,15,16] $CaAlSiN_3:Eu^{2+}$ PiG with a matrix glass of ZnO–B_2O_3–Ba_2O_3–Al_2O_3 have been studied at different holding times.[12] The results showed that the quantum efficiency decreases gradually with increasing holding time, which was ascribed to the oxidation of Eu^{2+} to Eu^{3+}. Mn^{4+}-doped phosphor is another superior red luminescent material owing to its suitable blue-light excitation and strong red-light emission at 600–700 nm. Mn^{4+}-doped phosphor-in-glass is also being widely studied at present. The erosion behavior of $3.5MgO{\cdot}0.5MgF_2{\cdot}GeO_2:Mn^{4+}$ red phosphor-in-glass with a TeO_2–ZnO–Na_2O–Al_2O_3 glass precursor was

[a]*School of Energy and Machinery Engineering, Jiangxi University of Science and Technology, Nanchang 330006, P. R. China. E-mail: tea_xia@126.com; Tel: +86 13970736437*
[b]*School of Materials Science and Engineering, Jiangxi University of Science and Technology, Ganzhou 341000, P. R. China*
[c]*Key Laboratory of Rare Earth Luminescence Materials and Devices of Jiangxi Province, Ganzhou 341000, P. R. China*

studied. The luminescence intensity gradually decreased when the sintering temperature increased from 525 to 625 °C,[17] implying that increase in temperature promotes the erosion of phosphor. For the PiG material of K_2SiF_6:Mn^{4+},Mn^{4+} was confirmed to be partially reduced and the luminescence intensity decreased under the process of co-sintering K_2SiF_6:Mn^{4+} PiG with SnF_2–SnO_2–P_2O_5 matrix glass.[11] Additionally, a series of PiGs were prepared by embedding $Li_3Mg_2SbO_6$:Mn^{4+} and $Y_3Al_5O_{12}$:Ce^{3+} phosphors in TeO_2–ZnO–Sb_2O_3–Al_2O_3–Na_2O glass substrates. Favorable luminous properties were obtained resulting from the low sintering temperature and no obvious erosion reaction between the phosphors and the glass matrix.[18]

In summary, the erosion behaviors and luminous properties of red PiGs have been widely studied. A low co-sintering temperature, a short holding time, and a suitable glass composition can all decrease the degree of erosion of red phosphors and maintain their strong luminescence intensities. However, the detailed erosion behaviors affected by co-sintering temperature, co-sintering time, and glass composition have not been studied simultaneously and systemically. In our previous work, an $Sr_4Al_{14}O_{25}$:Li^+,Mn^{4+} (SAO) phosphor with superior luminescence was synthesized.[19] In this work, SAO phosphor-in-glass films were prepared using a low-temperature sintering technique. A B_2O_3–Bi_2O_3–Al_2O_3–CaO glass system precursor was adopted due to the advantages of high transmittance, low melting point, and relatively stable structure, which are conducive to light transmittance and a reduction in phosphor erosion caused by high temperature.[20] The erosion behavior and luminescence property were systemically studied, and a series of valuable conclusions were obtained.

2. Experimental steps

2.1 Sample preparation

A series of precursor glasses, $x$$B_2O_3$–(85 − x)Bi_2O_3–5Al_2O_3–10CaO (x = 40, 45, 50, 55, 60), were prepared by a rapid melt quenching technique. The analytically pure grade H_3BO_3, Bi_2O_3, Al_2O_3 and CaO powders were thoroughly mixed and fully ground in an agate mortar for 30 min. The powders were then placed in an alumina crucible and melted at 950 °C for 1.5 h in a muffle furnace under air. The melt was quickly poured into pre-prepared deionized water to quench into a cullet, and the cullet was dried and milled into glass powder with the appropriate particle size. The binder, composed 99% (mass fraction) deionized water and 1% hydroxyethylene cellulose, was put in a glass beaker at 60 °C for 1 h with constant stirring. The mixtures (20 wt% SAO phosphors and 80 wt% glass powder) were mixed with the binder solution and stirred at 1000 rpm for 30 min to obtain a paint-like slurry. The slurries were then manually scraped onto a substrate of common soda-lime-silicate glass (15 × 10 × 1.2 mm^3) using a knife coater to control the thickness. The obtained samples were kept warm at 500 °C for 3 h to remove organic matter from the slurry. The obtained samples were then co-sintered under air at 570 °C for 30 min and naturally cooled. A series of SAO phosphor-in-glass films with precursor glasses containing different $x$$B_2O_3$ (x = 50, 55, 60) contents were prepared and labeled PG-x (x = 50, 55, 60). As a comparison, samples with pure glass frits (without any phosphor) and with different $x$$B_2O_3$ contents on soda-lime-silicate glass were prepared by the same technique and labeled G-x (x = 40, 45, 50, 55, 60).

2.2 Performance characterization

The glass transition temperature (T_g) was measured and the DSC experiment simulation was performed using a differential scanning calorimeter (EXSTAR6000) in the temperature range of 300–600 °C with a programmed heating rate of 10 °C min^{-1}. The infrared spectra were recorded in the range 400–1600 cm^{-1} using an FT-IR spectrometer (Agilent Cary-630). The crystalline/amorphous states were determined using an X-ray diffractometer (Bruker D8 Advance) with Cu K radiation in the 2θ range of 10–80° at a scanning rate of 2° min^{-1}. Morphologies were examined using a scanning electron microscope (Sigma 500) equipped with an energy dispersive X-ray spectroscopy (EDS) system. Excitation/emission spectra and fluorescence lifetime were measured using an FLS980 fluorimeter with a xenon flash lamp as the excitation source. Quantum efficiency (QE) was obtained using an FLS980 equipped with an integrating sphere. The temperature-dependent luminescence spectra were collected using an intensified multichannel spectrometer (MCPD-7000) in the temperature range 25 to 175 °C with a step size of 25 °C at a heating rate of 10 °C min^{-1} and holding each temperature for 5 min.

3. Results and discussion

3.1 Phase analysis

The XRD patterns of samples G-x (x = 40, 45, 50, 55, 60) and PG-x (x = 50, 55, 60) at different co-sintering temperatures of 570 and 590 °C are shown in Fig. 1. As can be seen from Fig. 1a, crystallization is observed in the samples G-40 and G-45, while the others show an amorphous structure. The sample G-40 exhibits a distinct crystalline phase. Although some small undesirable peaks appear in the patterns, the main substance is probably $Bi_4B_2O_9$ as compared with the standard card.[21] The low transparency of G-40 (the inset of Fig. 1a) also demonstrates glass crystallization behavior. The crystallization can be attributed to a decrease in the compactness of the glass structure and an increase in non-bridging oxygen with decreasing content of B_2O_3 (increasing the content of Bi_2O_3), which facilitates the combination of [BO_3] bonds and Bi^{3+} to produce a new phase of $Bi_4B_2O_9$. To avoid glass crystallization in the co-sintering process of the PiGFs, the samples PG-50, PG-55 and PG-60 were adopted for the subsequent studies.

The corresponding XRD spectra are shown in Fig. 1b. The figure reveals that PG-55 and PG-60 show obvious diffraction peaks originating from the SAO phosphor, whereas PG-50 shows an almost amorphous state. The slightly stronger peak intensity of PG-55 compared with that of PG-60 is probably

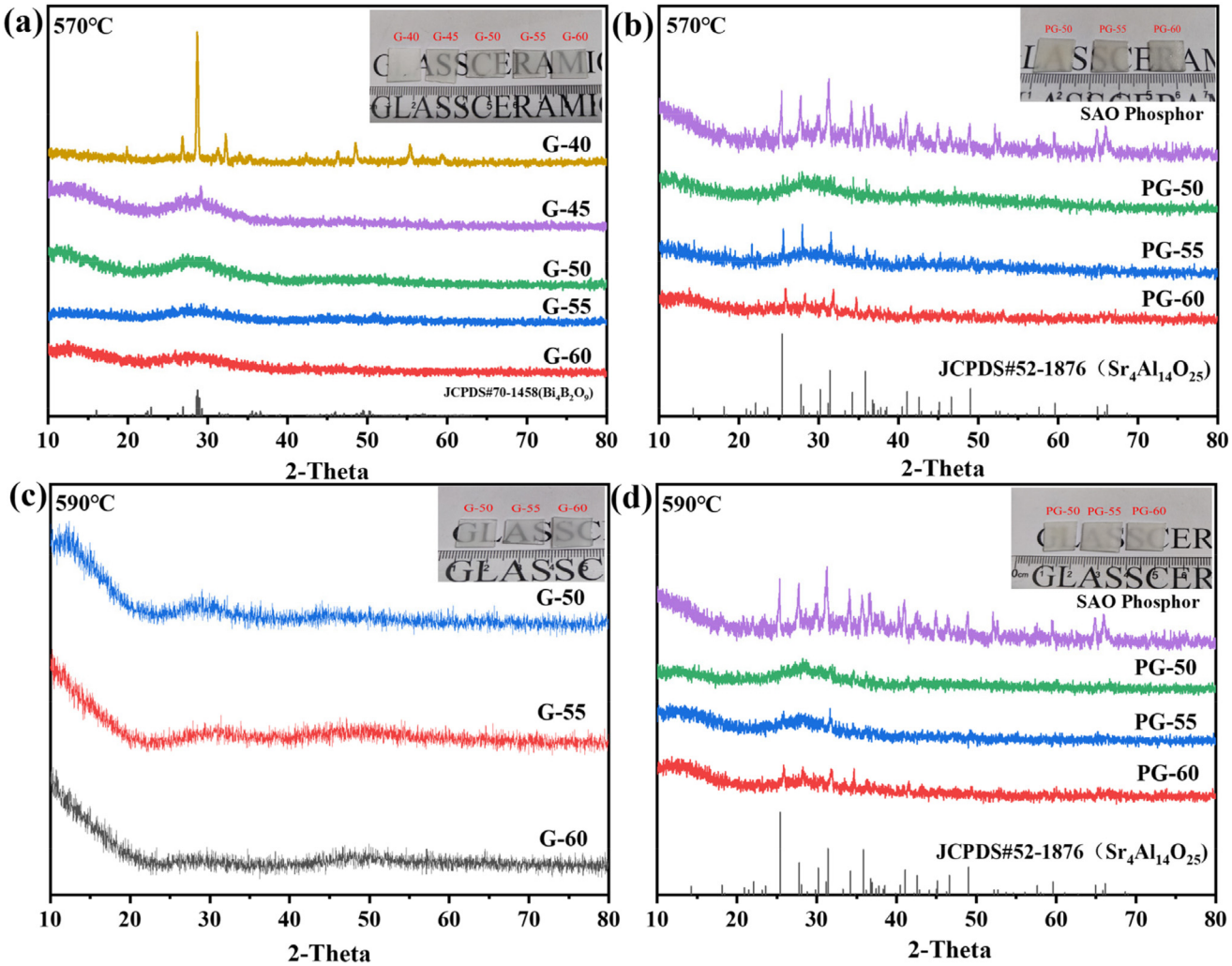

Fig. 1 XRD patterns of G-*x* (*x* = 40, 45, 50, 55, 60) and PG-*x* (*x* = 50, 55, 60) at different co-sintering temperatures of 570 °C (a and b) and 590 °C (c and d); the insets are physical images.

owing to measurement error. The disappearance of a few diffraction peaks in PG-55 compared with the SAO phosphor is probably attributed to the preferred orientation and slight erosion. These results indicate that the degree of erosion of SAO decreases with an increase in B_2O_3 content, and 55% B_2O_3 (mole fraction, the same as below) is a suitable value, which is also due to the decrease in the compactness of the glass structure and the increase in non-bridging oxygen. Fig. 1c and d show the XRD spectra of G-50, G-55, G-60 and the corresponding PiGFs at the co-sintering temperature of 590 °C, respectively. Fig. 1c shows that the three samples exhibit good amorphous states and high transparency, which helps the subsequent preparation of PiGFs. Fig. 1d shows that the diffraction peaks decrease with decreasing B_2O_3 content, indicating the occurrence of obvious erosion in samples PG-50 and PG-55 at 590 °C. This result can be attributed to the decrease in glass viscosity at high temperature and the increase in activity for non-bridging oxygen that promotes the chemical reactions. However, PG-60 shows a rough surface at both 570 and 590 °C, simultaneously ascribed to the high glass softening temperature, which would decrease the light emitting efficiency (as shown in the insets). Therefore, 55% B_2O_3 and 570 °C are the optimal parameters.

Fig. 2a shows the DSC curves of the precursor glasses. The glass transition temperature (T_g) obviously and gradually increases from 420 to 496 °C with increasing B_2O_3 content from 40 to 60%. This result is ascribed to the decrease in non-bridging oxygen and increase in compactness of the glass structure, which causes the thermal expansion coefficient to increase gradually. The G-40 sample shows a prominent exothermic peak, indicating that glass crystallization behavior has occurred. This is consistent with the results of the above XRD analysis (Fig. 1a). To explore whether the phosphor reacted with the precursor glasses during the co-sintering process, simulation experiments on the PiGFs were performed according to the preparation conditions (at 570 °C for 30 min) using a DSC instrument. The related results are shown in Fig. 2b. The PG-50 sample shows a slight bulge at 10–20 min,

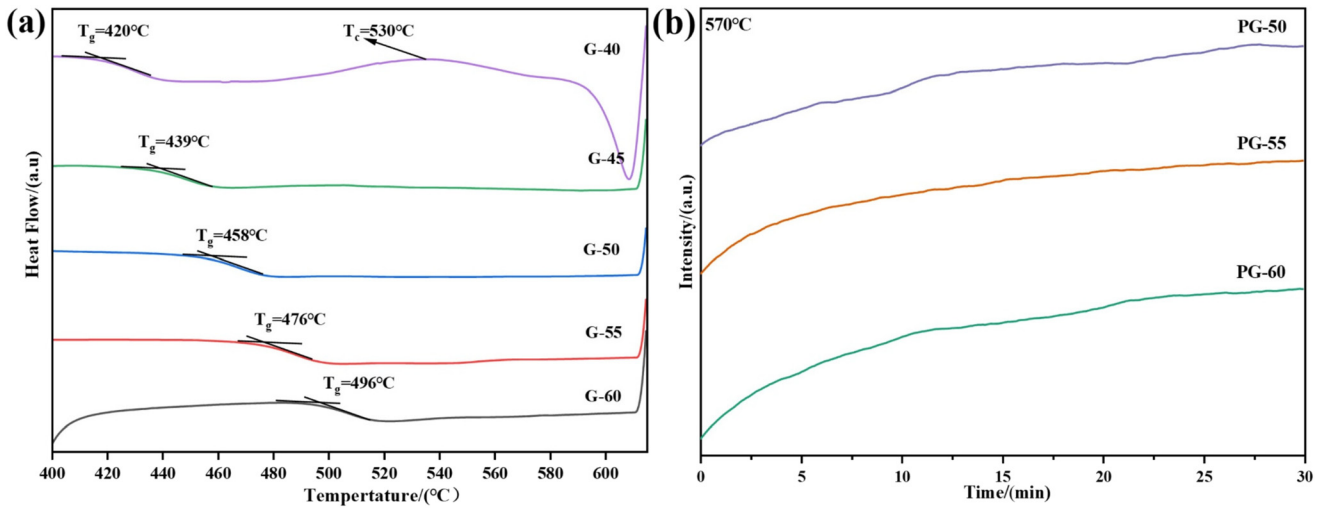

Fig. 2 DSC curves of (a) precursor glasses and (b) simulation experiments for PiGFs.

whereas PG-55 and PG-60 show flat lines without an obvious endothermic/exothermic peak, indicating that the SAO phosphors probably react with the precursor glasses in PG-50 with no reactions in the others. This result is also consistent with the findings in Fig. 1b.

3.2 Glass structure

The FTIR transmission spectra of the precursor glasses are shown in Fig. 3. The broad bands from 1100 cm^{-1} to 1500 cm^{-1} are ascribed to the B–O bond stretching vibrations in $[BO_3]$ of pentaborate, pyroborate, and *o*-borate.[22,23] Among these, the bands from 1100 cm^{-1} to 1200 cm^{-1} are related to the asymmetric stretching vibrations of the B–O bond in the $[BO_3]$ unit.[21] The shoulders at about 1025 cm^{-1} are assigned to B–O stretching vibrations in the $[BO_4]$ unit in tri-, tetra-, and pentaborates.[24,25] The above bands obviously move towards higher wavenumber with increasing B_2O_3 content (decreasing Bi_2O_3), which is ascribed to the greater quantities of glass network formed of $[BO_3]$ and $[BO_4]$. Thus, the compactness of the glass structure increases gradually. The bands at about 877 cm^{-1} are attributed to the symmetric stretching vibration of the Bi–O bond in the $[BiO_3]$ group. The bands at 699 cm^{-1} and 613 cm^{-1} are associated with the bending vibration of the B–O–B bond in the $[BO_3]$ group.[25] The waves at about 483 cm^{-1} are derived from the vibration of the B–O bond or the Bi–O–Bi bond in the $[BiO_6]$ octahedron.[26]

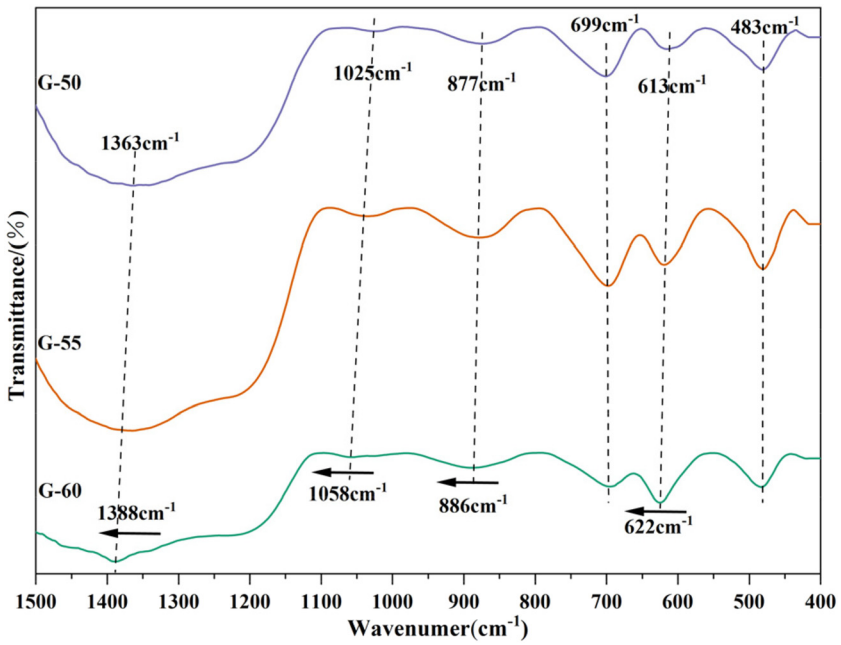

Fig. 3 FTIR transmission spectra of precursor glasses.

3.3 Morphology and elemental analysis

Fig. 4a shows the SEM image of the surface morphology of G-40. The obviously uneven surface and graininess of the substance can be observed, indicating glass crystallization in the precursor glass. The related result of EDS analysis on point scanning is shown in Fig. 4b. The elements Bi and O as well as Ca and Al are obtained in the sample, though B is not detected due to its light molecular mass. However, the $n_{Bi/Ca}$ and $n_{Bi/Al}$ values are 24.31/5.01 (4.85 : 1) and 24.31/13.4 (1.81 : 1), respectively, which show a significant difference from that of the glass composition (9 : 1, 4.5 : 1). This result demonstrates that crystalline phases have been produced. Fig. 4c–e show the SEM images of the surface morphology of G-50, G-55, and G-60. Compared with G-40, these samples show relatively smooth surfaces, with crystalline phases. However, some particles appear on the surface of G-60, due to some unmelted glass powder at high temperature; thus, the G-60 sample shows a rougher surface. This conclusion is consistent with the physical image shown in the inset of Fig. 1b.

The SEM images of PG-50, PG-55 and PG-60 and the corresponding spot/line scanning results are shown in Fig. 5. As can be seen from Fig. 5a–c, the samples of PG-50 and PG-55 exhibit smooth surface morphologies, while PG-60 has a relatively rough morphology. These results are consistent with those in Fig. 4c–e. To intuitively compare the degree of erosion of the SAO phosphors in the precursor glass, the spot/line scanning spectra and EDS results are illustrated in Fig. 5d and e. The result for PG-50 (Fig. 5d) shows only the elements Sr, Al, and O ascribed to SAO appearing in spot 1 (Li not being found is also ascribed to its light molecular mass). However, the element Sr, which is not contained in the glass composition, emerges in spot 2, as shown in Fig. 5e. In comparison, Fig. 5f and g (the results for PG-55) show that no extra element emerges in the region of the SAO phosphors and precursor glass. The $n_{Sr/Al}$ values for PG-50 and PG-55 are 0.32 and 0.34, respectively. Although the values are approximately equal to that of SAO ($n_{Sr/Al}$ = 4/14 = 0.29), the smaller value for PG-50 indicates a small amount of Sr element melted into the glass region. Fig. 5h and i show the line scanning spectra of PG-50 and PG-55. Sr and Al in the SAO phosphors exhibit a dramatic decrease, while Bi and Ca in the precursor glass show a steep increase. However, the slope of PG-50 is smaller than that of PG-55. All the above results show that the degree of erosion of SAO phosphors decreases and the surface roughness of PiGFs increases with increasing B_2O_3 content. 55% B_2O_3 is the optimal value.

To investigate the impact of soaking time on the surface smoothness of the PiGFs, SEM images of PG-55 at different co-sintering times of 20, 25 and 30 min (named PG-55-20, PG-55-25 and PG-55, respectively) are shown in Fig. 6. Clearly, the surface of PG-55-20 (Fig. 6a) exhibits clear unmelted particles and a higher surface roughness. With increasing soaking time, the unmelted particles on the surface of PG-55-25 (Fig. 6b) are significantly reduced and the surface roughness decreases; the unmelted parts disappear and the surface becomes smooth in the PG-55 (Fig. 6c). The above results indicate that the surface roughness of the PiGFs decreases with increasing soaking time and that 30 min is the suitable time.

4. Optical properties

Fig. 7a and b show the photoluminescence excitation (PLE) and photoluminescence (PL) spectra of the PiGs, respectively. As shown in Fig. 7a, the peaks at about 295 nm are ascribed to

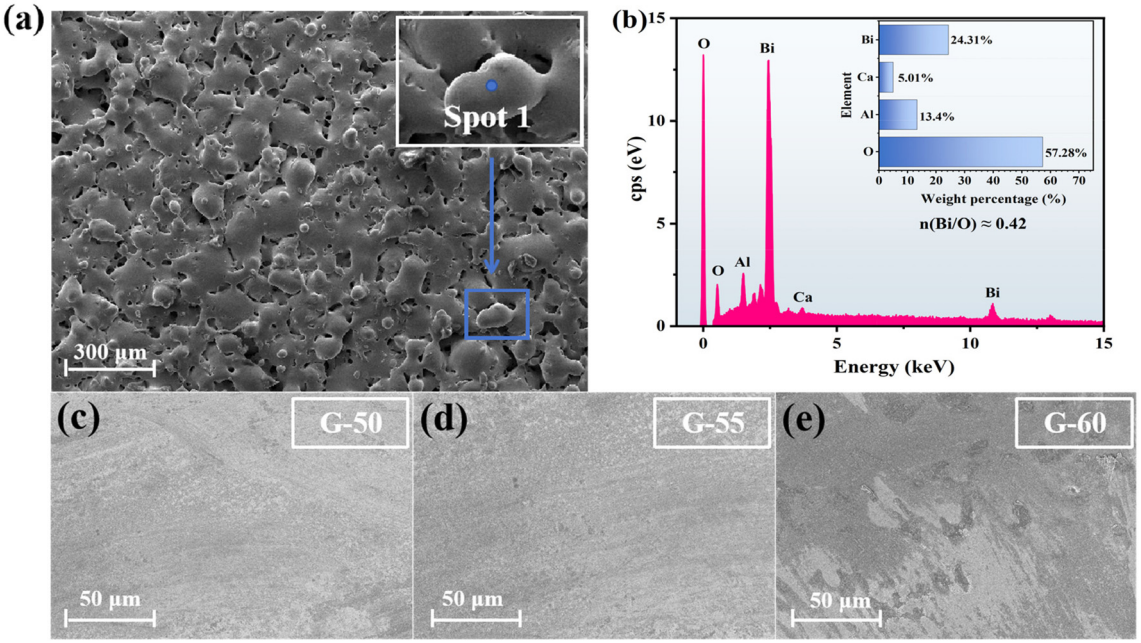

Fig. 4 (a and b) SEM and EDS images of G-40, (c–e) SEM images of G-50, G-55 and G-60 surfaces.

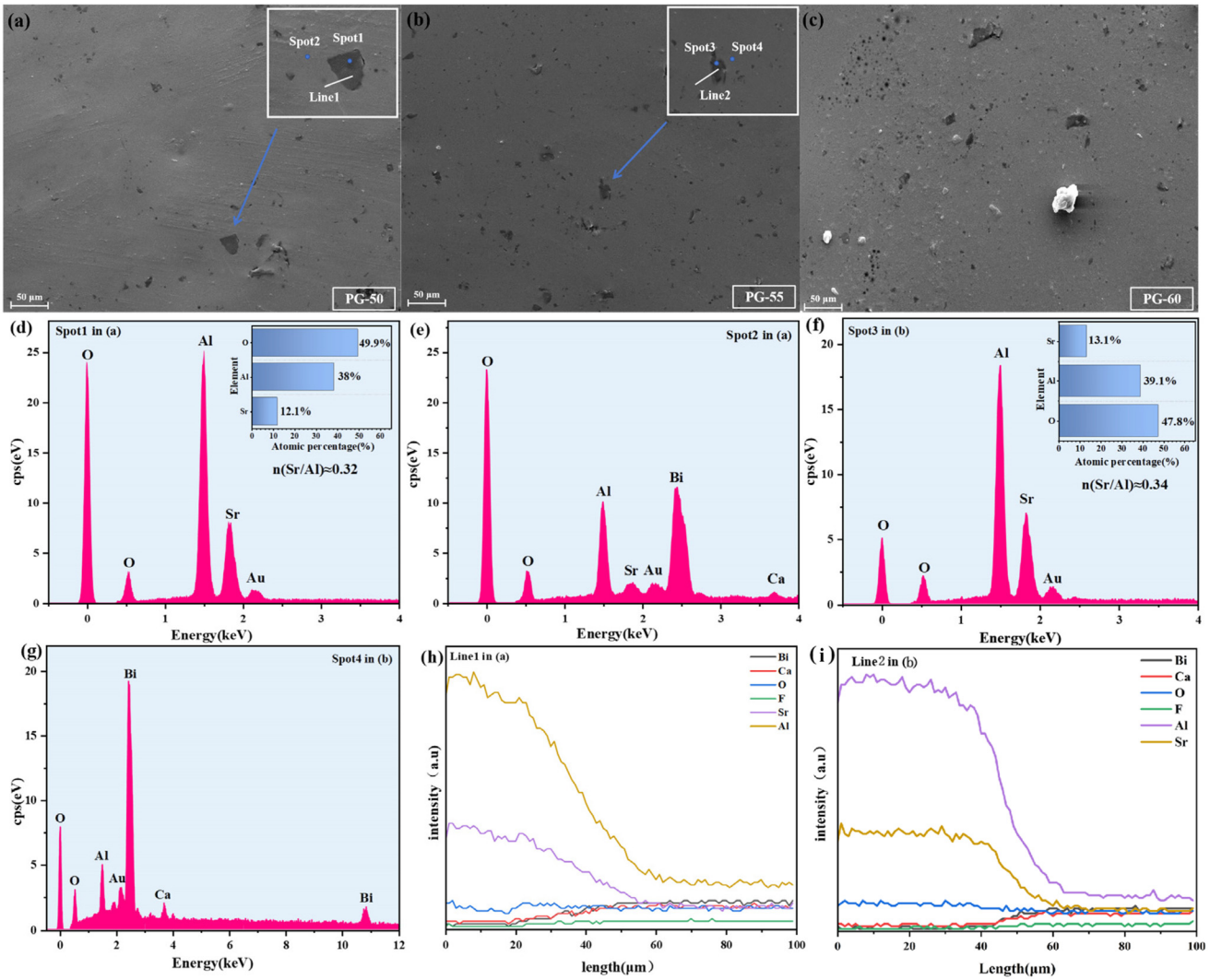

Fig. 5 (a–c) SEM images of PG-50, PG-55 and PG-60; the insets are locally enlarged images. (d–i) EDS of point and line scanning of the samples.

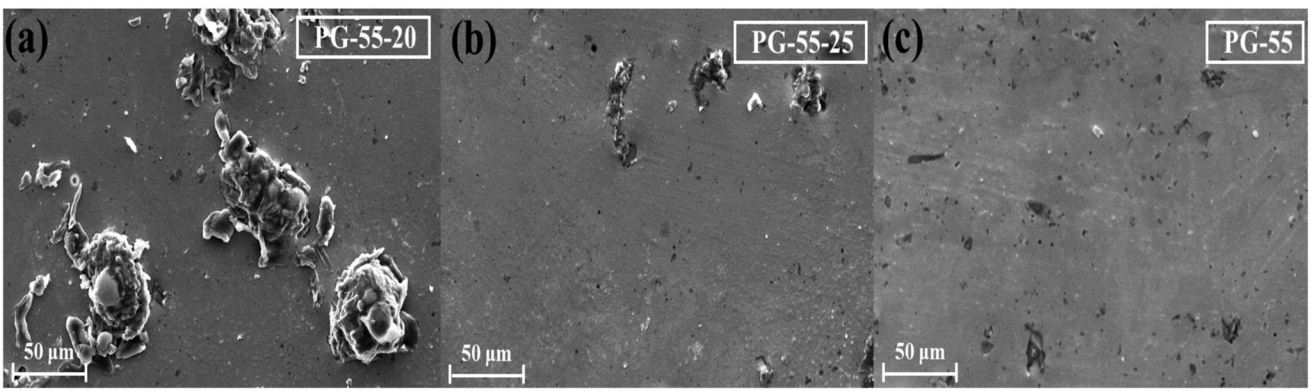

Fig. 6 SEM images of PG-55 at different preservation times: (a) 20 min, (b) 25 min, (c) 30 min.

the charge transfer band of Mn^{4+}–O^{2-}. The band at about 375 nm originates from the $^4A_{2g} \rightarrow {}^4T_{1g}$ transition of Mn^{4+}, while the band centered at 445 nm is attributed to the $^4A_{2g} \rightarrow {}^4T_{2g}$ transition of Mn^{4+}. The intensity of the band at 375 nm for GC-50 is significantly weaker than the others, and the peak position shifts to longer wavelength, which is possibly due to

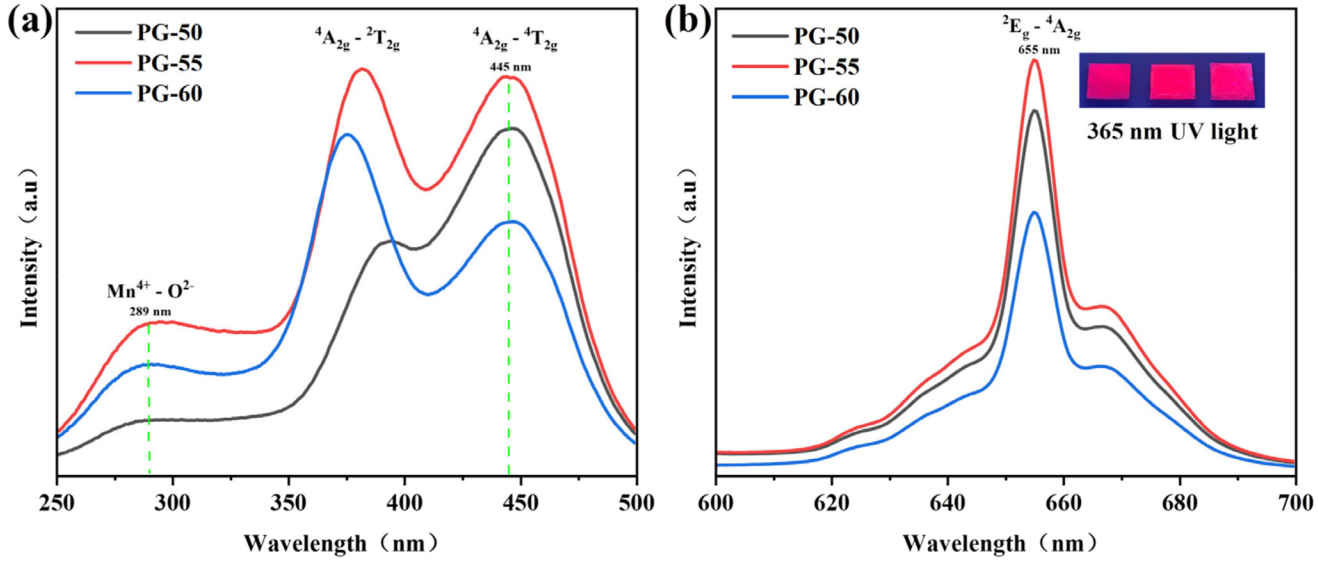

Fig. 7 PLE (a) and PL (b) spectra of PG-50, PG-55 and PG-60 (the inset shows physical images).

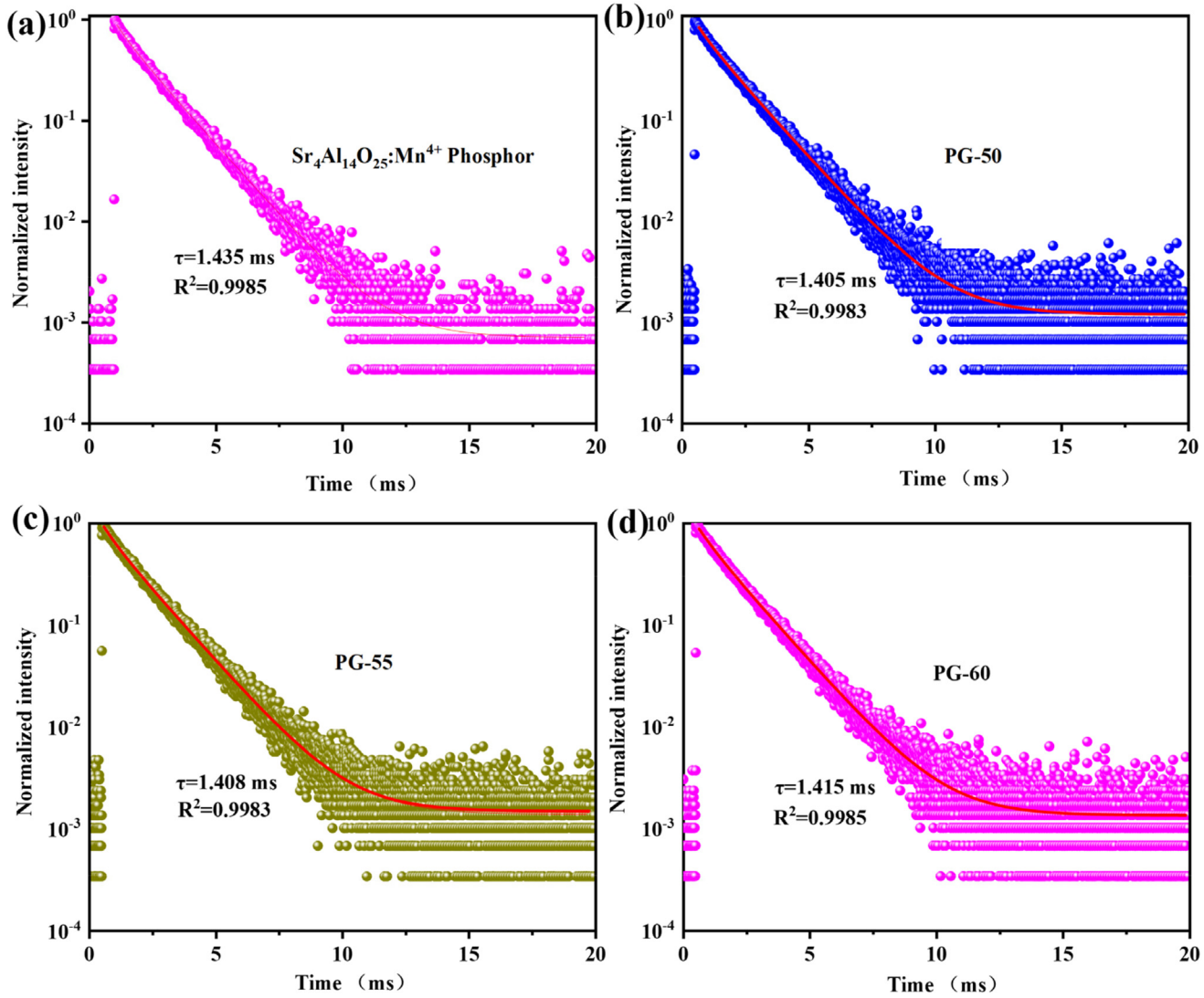

Fig. 8 (a–d) Decay curves of SAO Phosphor, PG-50, PG-55 and PG-60.

the large degree of erosion of the SAO phosphor and the change to the crystal field surrounding Mn^{4+}. The peaks centered at 652 nm are ascribed to the $^2E_g \rightarrow {}^4A_{2g}$ transition of Mn^{4+}, as shown in Fig. 7b. The inset shows physical images of the PiGs under excitation by 365 nm UV light, indicating that the as-prepared PiGs show superior red-light emission. Clearly, the PL and PLE show that the luminous intensity increases and then decreases with increasing B_2O_3 content, with 55% B_2O_3 being the optimal value. The increase is probably due to the decrease in the degree of erosion on the SAO phosphor, while the decrease is due to the decrease in surface smoothness with increasing B_2O_3 content—so the light scattering increases.

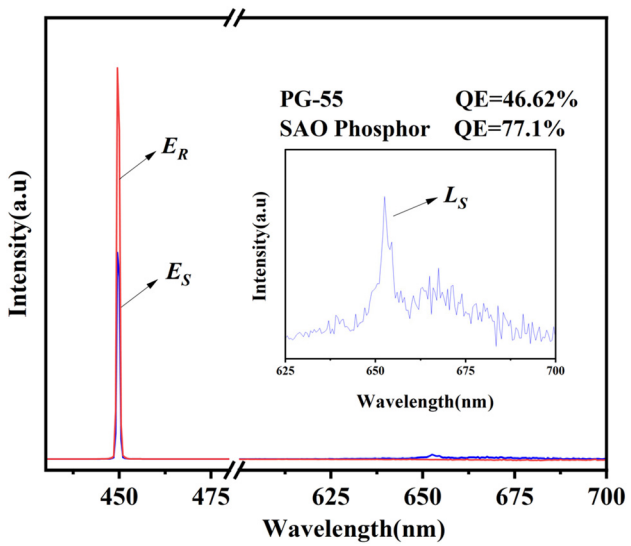

Fig. 9 Quantum yield of PG-55.

Fig. 8 shows the decay curves of the PiGFs. Based on our previous study,[27] the fluorescence lifetimes were calculated using double exponent fitting using the following formula (1):[28]

$$I(t) = A_1 e^{\frac{-t}{\tau_1}} + A_2 e^{\frac{-t}{\tau_2}} \quad (1)$$

where A_1 and A_2 are fitting constants, τ_1 and τ_2 are exponential components, I is luminescence intensity, and t is time. Then, the average fluorescence lifetimes were calculated using the conversion formula (2):

$$\tau = \frac{A_1\tau_1^2 + A_2\tau_2^2}{A_1\tau_1 + A_2\tau_2}. \quad (2)$$

The lifetime of the raw material of the SAO phosphor was calculated and the value is 1.435 ms, while those of PG-50, PG-55 and PG-60 are 1.405, 1.408 and 1.415 ms, respectively. Overall, the lifetime values of the PiGFs are slightly smaller than that of the SAO phosphor, which is ascribed to minor erosion of the SAO phosphor in the PiGFs. Generally, the higher the heat generated, the larger the non-radiative transition, which will reduce fluorescence lifetime. The lifetime value increases with an increase in B_2O_3 content from 50 to 60%, indicating that the non-radiative transition probability decreases gradually. This result demonstrates that to some extent the degree of erosion of the SAO phosphor decreases with increasing B_2O_3 content.

The quantum efficiencies (QE) of PG-55 and its raw material were measured, and the results are shown in Fig. 9. The values were calculated with the following formula (3):[29]

$$\mathrm{IQE} = \int L_S / \left(\int E_R - \int E_S \right) \quad (3)$$

where L_S denotes the PL spectra collected by an integrating sphere. E_R and E_S denote the PLE spectra of $BaSO_4$ and the

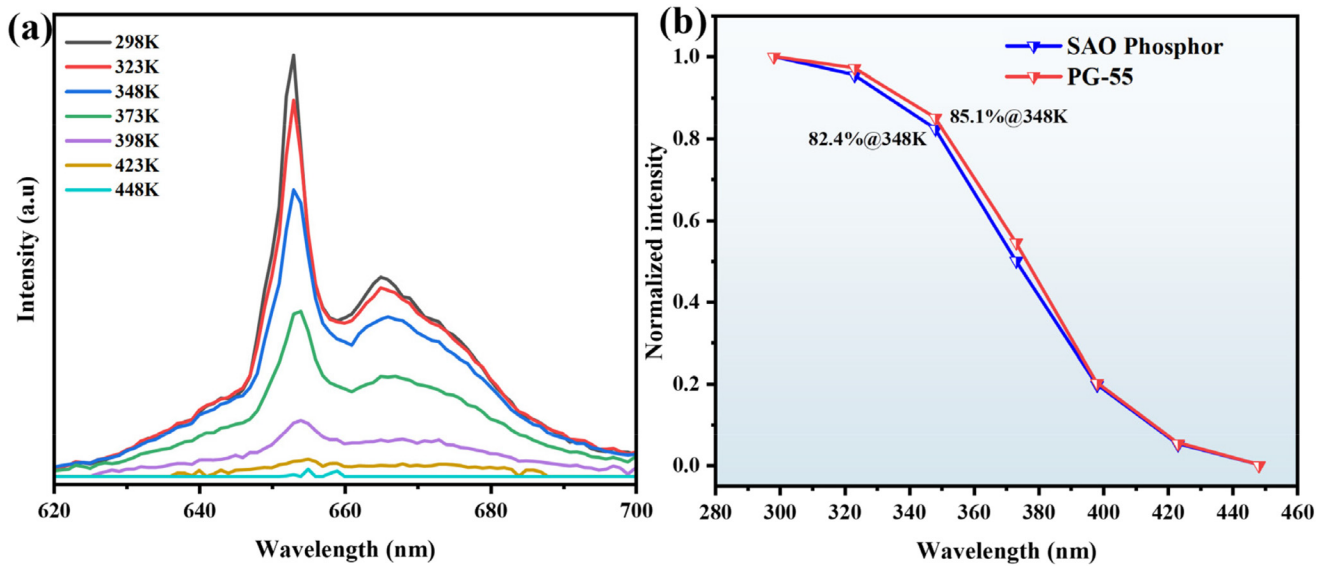

Fig. 10 (a) Temperature-dependent PL spectra and (b) relative PL intensity of PG-55.

standard reference, respectively. The results show that the QE value of PG-55 is 46.62%, which is smaller than that of the raw material (77.1). This result can possibly be ascribed to the slight erosion of SAO phosphors. Light scattering between the phosphor and precursor glass originating from the difference in refractive indexes is another possible reason.

Fig. 10 shows the temperature-dependent luminescence spectra of PG-55 under excitation of 450 nm. The luminous intensity decreases gradually with increasing temperature. This result can be ascribed to the increase in main lattice vibration. More excited electrons are transferred to the non-radiative transition, resulting in a decrease in luminous intensity.[30,31] However, PG-55 still maintains 85.1% of its initial intensity at 348 K (75 °C), while the SAO phosphor retains 82.4%. This increase can probably be ascribed to the high thermal conductivity of glass. The curves show rapid decreases when the temperature exceeds 348 K (75 °C), which is due to the intrinsic poor thermal quenching resistance of SAO phosphors.[32,33] Generally, the applied temperature of a WLED device with a radiator is within 75 °C in the field of medium-power illumination.[19] Therefore, the as-prepared PiGF still shows positive application prospects.

5. Conclusions

In brief, novel $Sr_4Al_{14}O_{25}:Li^+,Mn^{4+}$ (SAO) phosphor-in-glass films (PiGFs) with bismuth borate glass precursors were prepared *via* a low-temperature sintering technique. The erosion behavior between the SAO phosphors and precursor glasses, as well as the luminous properties of the PiGFs were systematically investigated. Crystallization was observed in the precursor glass with 40% and 45% B_2O_3 content at 570 °C for 30 min, with the crystalline phase being mainly $Bi_4B_2O_9$. The glass transition temperature gradually increased from 420 to 496 °C with an increase in B_2O_3 content from 40 to 60%. The DSC simulation and experimental results show that the degree of erosion of SAO phosphors decreases with an increase in B_2O_3 content from 50 to 60% and an increase in the co-sintering temperature from 570 to 590 °C. However, the glass surface smoothness of the PiGFs decreases with increasing B_2O_3 content. 55% B_2O_3 and 570 °C are the optimal parameters. The PL and PLE of the PiGFs show that the luminous intensity increases and then decreases with increasing B_2O_3 content, and 55% B_2O_3 is also the optimal value. The PiGF has a quantum efficiency of 46.62%, and the luminous intensity maintains 85.1% of its initial intensity at 348 K, which is larger than that of the raw materials. The above results indicate that the as-prepared SAO-PiGF is a promising candidate in the field of medium-power warm WLEDs.

Author contributions

Yunzheng Liu: conceptualization, methodology, investigation, writing – original draft. Haoyu Yang and Haohui Jiang: conceptualization, investigation. Daoyuan Ma: data curation, writing – original draft. Wenfa Fang: resources, data curation. Libin Xia: supervision, writing – review & editing, project administration, funding acquisition.

Data availability

All the data for this article can be found in the article.

Conflicts of interest

The authors declare no competing financial interest.

Acknowledgements

This work was supported by the National Natural Science Foundation of China (52062017) and Jiangxi Provincial Natural Science Foundation (20232BAB204013).

References

1 J. Kaewkhao, K. Boonin, P. Yasaka and H. J. Kim, *Mater. Res. Bull.*, 2015, **71**, 37–41.
2 R.-Q. Su, Q.-Q. Zhu, H. Mei, S. Fang, Y. Zhai, P. Liang, H. Zhang and L. Wang, *J. Lumin.*, 2023, **263**, 120080.
3 Y. Zhang, B. Chen, X. Zhang, Y. Cao, J. Zhang, S. Xu, X. Li, H. Yu, D. Gao, X. Sha, L. Wang, X. Chen and H. Lin, *Chem. Eng. J.*, 2023, **467**, 143467.
4 H. Lin, T. Hu, Y. Cheng, M. Chen and Y. Wang, *Laser Photonics Rev.*, 2018, **12**, 1700344.
5 W. J. Chung and Y. H. Nam, *ECS J. Solid State Sci. Technol.*, 2019, **9**, 016010.
6 X. X. Guo, J. H. Wei, J. B. Luo, Z. L. He, Z. Z. Zhang, J. H. Chen and D. B. Kuang, *Adv. Opt. Mater.*, 2023, **12**, 2301914.
7 L. Xia, Q. Xiao, X. Ye, W. You and T. Liang, *J. Am. Ceram. Soc.*, 2018, **102**, 2053–2065.
8 L. Wang, J. Zhang, L. Wang, Y. Liang, F. Xu, L. Xu, X. Liang, Q. Chen and W. Xiang, *J. Mater. Chem. C*, 2022, **10**, 7167–7175.
9 Z. Liu, P. Hu, H. Jiang, P. Sun, Y. Liu, Z. Luo, J. Xu, Z. Huang and J. Jiang, *J. Mater. Chem. C*, 2021, **9**, 3522–3530.
10 Y. Zhang, B. Chen, X. Zhang, J. Zhang, S. Xu, H. Yu, X. Li, Y. Cao, Y. Wang, X. Wang, D. Gao, X. Sha and L. Wang, *Ceram. Int.*, 2022, **48**, 22994–23001.
11 S. Si, L. Huang, X. Zhang and J. Wang, *Adv. Photonics Res.*, 2021, **3**, 2100146.
12 Q.-Q. Zhu, X. Xu, L. Wang, Z.-F. Tian, Y.-Z. Xu, N. Hirosaki and R.-J. Xie, *J. Alloys Compd.*, 2017, **702**, 193–198.
13 Y. Zhang, Z. Zhang, X. Liu, G. Shao, L. Shen, J. Liu, W. Xiang and X. Liang, *Chem. Eng. J.*, 2020, **401**, 125983.

14 Y. Peng, R. Li, H. Cheng, Z. Chen, H. Li and M. Chen, *J. Alloys Compd.*, 2017, **693**, 279–284.
15 H. Zhang, Y. Li, J. Ling, J. Yang, M. Jin, W. Xu, Y. Zhou and M. Hong, *Ceram. Int.*, 2023, **49**, 23871–23877.
16 Z. Weng, X. Yi, Y. Tang, Y. Tian, J. Chen, D. Zhao, S. Zhou and Y. Lin, *Opt. Mater.*, 2021, **115**, 111043.
17 Y. Peng, Y. Mou, Y. Zhuo, H. Li, X. Wang, M. Chen and X. Luo, *J. Alloys Compd.*, 2018, **768**, 114–121.
18 J. Zhong, X. Chen, D. Chen, M. Liu, Y. Zhu, X. Li and Z. Ji, *J. Alloys Compd.*, 2019, **773**, 413–422.
19 X. Wang, D. Ma, Y. Liu, B. Song, L. Long and L. Xia, *Dalton Trans.*, 2023, **52**, 13983–13990.
20 Y. Liang, X. Zhou, Y. Fu, H. Hou, F. Zou, C. Wu and L. Xia, *J. Non-Cryst. Solids*, 2022, **578**, 121339.
21 L. Xia, X. Ye, H. Ge, Y. Qiang, Q. Xiao, Q. Zhang and Z. Tong, *Ceram. Int.*, 2017, **43**, 17005–17014.
22 D. D. Ramteke, H. C. Swart and R. S. Gedam, *Phys. B*, 2016, **480**, 111–115.
23 K. Swapna, S. Mahamuda, A. Srinivasa Rao, S. Shakya, T. Sasikala, D. Haranath and G. Vijaya Prakash, *Spectrochim. Acta, Part A*, 2014, **125**, 53–60.
24 Z. Y. Yao, D. Möncke, E. I. Kamitsos, P. Houizot, F. Célarié, T. Rouxel and L. Wondraczek, *J. Non-Cryst. Solids*, 2016, **435**, 55–68.
25 M. Anand Pandarinath, G. Upender, K. Narasimha Rao and D. Suresh Babu, *J. Non-Cryst. Solids*, 2016, **433**, 60–67.
26 C. Zhang, Y. Shi, K. Lu, X. Wang, H. Yuan, R. Chen, J. Qi and T. Lu, *Opt. Express*, 2023, **31**, 28963–28978.
27 X. Wang, Q. Jiang, Z. Wang, B. Song, H. Hou, L. Xu and L. Xia, *J. Mater. Chem. C*, 2022, **10**, 7909–7916.
28 S. Kaur, A. K. Vishwakarma, N. Deopa, A. Prasad, M. Jayasimhadri and A. S. Rao, *Mater. Res. Bull.*, 2018, **104**, 77–82.
29 G. Li, G. Liu, Q. Mao, G. Du, X. Li, Y. Zhu, T. Yang, H. Yu, Z. Ji and J. Zhong, *Ceram. Int.*, 2021, **47**, 27609–27616.
30 Monika, R. S. Yadav, A. Bahadur and S. B. Rai, *RSC Adv.*, 2019, **9**, 40092–40108.
31 R. S. Yadav, S. J. Dhoble and S. B. Rai, *Sens. Actuators, B*, 2018, **273**, 1425–1434.
32 M. Peng, X. Yin, P. A. Tanner, M. G. Brik and P. Li, *Chem. Mater.*, 2015, **27**, 2938–2945.
33 L. Luo, R. Liu, Y. Liu, W. Zhuang, Y. Li and T. Gao, *Inorg. Chem. Commun.*, 2020, **118**, 107972.